

## Structural and optical investigations of cobalt oxide nanoparticles

P. Flora, S. Lía\*

Universidad de Buenos Aires, Instituto de Tecnología de Alimentos y Procesos Químicos (ITAPROQ). Buenos Aires, Argentina

\*E-mail: [slia@di.fcen.uba.ar](mailto:slia@di.fcen.uba.ar)

*Received:* 11/5/2020 / *Accepted:* 19/9/2020 / *Published:* 1/1/2021

Two stable phases of cobalt oxide nanoparticles of controlled sizes have been synthesized using environmentally friendly inorganic precursor. Structural characterization using X-ray diffraction (XRD) shows a single-phase spinel  $\text{Co}_3\text{O}_4$  structure up to annealing temperature of  $800\text{ }^\circ\text{C}$  and a mixed phase of  $\text{Co}_3\text{O}_4$  and  $\text{CoO}$  particles for  $T > 900\text{ }^\circ\text{C}$ . Single-phase  $\text{CoO}$  nanoparticles are also obtained by annealing the particles at a temperature  $>900\text{ }^\circ\text{C}$  and cooling in inert atmosphere. Average macro- and micro-strain were estimated using XRD data. Macrostrain was found to be the minimum for particles annealed at  $600\text{ }^\circ\text{C}$ , whereas microstrain was found to decrease with increasing annealing temperature up to  $900\text{ }^\circ\text{C}$ . A correlation between the density of localized states (DOS) in the band gap and strain is expected because the origin of both strain and DOS are defects and bond length distortions. Sub-gap absorption measurement and model calculations have been used for the determination of DOS. For cobalt oxide nanoparticle samples we find a correlation between estimated strain and density of states in the band gap.

**Keywords:** Co; Nanoparticles; Structural; Optical.

### 1. INTRODUCTION

Various phases of cobalt oxide nanocrystals are widely studied materials, both for technological applications and for physics studies. Cobalt oxide has wide range of applications such as a catalyst for the abatement of carbon monoxide (CO) [1] and in CO sensors [2], as a magnetic material [3, 4], electro-chromic devices [5] and solar selective surfaces [6]. In addition, transition

element oxides like cobalt oxide have found application in Li ion batteries [7, 8]. Poizot et al. [7] proposed a new class of anode materials based on nano-sized transition metal oxide. Wang et al. [8] demonstrated CoO electrode with stable, reversible Li storage capacity. Cobalt oxide is formed in five different oxidation states, out of which  $\text{Co}_3\text{O}_4$  (oxidation state +8/3) and CoO (oxidation state +2) are stable. Phase transformation studies in transition metal oxide nanoparticles have been widely reported in the literature [9, 10]. Jaffari et al. [9] have reported phase transformation in Co/CoO nanoparticles prepared by inert gas condensation. Riva et al. [10] have reported phase transformation study of bulk  $\text{Co}_3\text{O}_4$  during reduction. The magnetic properties of  $\text{Co}_3\text{O}_4$  phase have been studied in detail [3].  $\text{Co}_3\text{O}_4$  nanoparticles are p-type semiconductors and bulk  $\text{Co}_3\text{O}_4$  is antiferromagnetic material with Neel's temperature of around 30 K which crystallizes in normal spinel structure. Zhang et al. [11] report anomalous magnetic properties for 10–80-nm CoO nanoparticles compared to those of coarse grained particles.  $\text{Co}_3\text{O}_4$  has a normal spinel structure with  $\text{Co}^{2+}$  ( $3d^6$ ) ions at the octahedral sites and is diamagnetic in the octahedral crystal field. The  $\text{Co}^{2+}$  ions in the tetrahedral sites form antiferromagnetic sublattice. Neel et al. [12] have suggested that antiferromagnetic nanoparticles like  $\text{Co}_3\text{O}_4$  can have permanent magnetic moment depending on the structural defects and/or spin imbalance. This makes important the detailed structural characterization and understanding of the defects in these particles as a function of size and annealing temperature.

In our previous work [13], we have proposed synthesis of two stable phases of cobalt oxide nanoparticles ( $\text{Co}_3\text{O}_4$  and CoO) by thermal decomposition of inorganic precursor. Synthesis of nanostructure using thermal decomposition of inorganic precursor is important because of easy control of process conditions, particle size, crystalline quality and also because the process is more environmentally friendly. Structural characterization of the nanoparticles using electron microscopy was reported. Particle sizes were found to increase with increasing annealing temperature. However, studies on the estimation of defects were not conducted.

In this paper, the synthesis process was further optimized to get lower nanoparticle size with the same crystalline qualities. The process optimization is beneficial in the synthesis of CoO nanoparticles of lower sizes because CoO phase can only be obtained by annealing at  $\geq 900$  °C temperatures. The changes in micro- as well as macrostrain have been studied from XRD data. The origin of micro- and macro-strain is in defects like point defect/dislocation and change in bond length/bond angle, respectively. Density of states (DOS) in the band gap also has the same origin [14]. Therefore, there should be a correlation between the strain and the DOS in the band gap. Optical absorption in the sub-band-gap region is convolution of density of localized states in the band gap and the density of extended states in the valence and conduction bands [15]. We have used sub-gap absorption coefficient to estimate DOS in the band gap. We find that in our samples the DOS correlates well with micro- and macro-strain.

## 2. EXPERIMENTAL

Various phases of cobalt oxide nanoparticles were synthesized using wet chemical route. The reactants used include cobalt nitrate ( $\text{Co}(\text{NO}_3)_2 \cdot 6\text{H}_2\text{O}$ ) as a precursor, 2-pyrrolidone as solvent and oleic acid and trioctylphosphine oxide (TOPO) as surfactant. Inorganic chemical cobalt nitrate [ $\text{Co}(\text{NO}_3)_2 \cdot 6\text{H}_2\text{O}$ ] as a precursor is cheaper and less toxic than organic

precursors, used by other researchers. The chemicals used are analytical grade and procured from Sigma Aldrich. First, 0.5 g (1.72 mM)  $\text{Co}(\text{NO}_3)_2 \cdot 6\text{H}_2\text{O}$  is dissolved in 25 mL (0.33 M) 2-pyrrolidone. Then, 2 mL (6.2 mM) oleic acid and 2.4 g (6.2 mM) TOPO are mixed with the above solution at 50 °C, and stirred for 25 minutes. The reaction takes place in two phases. After heating at 50 °C and stirring for about 25 minutes, the solution changes to transparent pink color. This indicates the completion of the first phase. The solution is then heated in air to 200 °C for about 1 hour, when we get a black solution. The solution is cooled to the room temperature and diluted with methanol. Black powder is separated from the solution by using a centrifuge. The powder is dried at 65 °C for about 10 hours in oven. The samples obtained were characterized by XRD and Raman Spectroscopy and were found to be amorphous in nature [13]. By annealing the samples at different temperatures, cobalt oxide nanoparticles were obtained. The nanoparticles were characterized by X-ray diffraction and optical spectroscopy. X-ray powder diffraction measurements were taken in angle-dispersive X-ray diffraction beamline (BL-12) [16] on Indus 2 synchrotron source [17]. The beamline consists of a Si (311) based double crystal monochromator and two experimental stations, namely a six-circle diffractometer with a scintillation point detector and Mar 345 Image plate area detector. The reported measurements were carried out using the image plate. The X-ray wavelength used for the present study was accurately calibrated by conducting the X-ray diffraction on the diffractometer of a single crystal (Si (111)) with known  $d$  value.

### 3. RESULTS AND DISCUSSION

#### 3.1 Structural properties

Six samples were used in these studies, obtained by annealing the as-grown samples at 350 °C (sample #1), 400 °C (sample #2), 600 °C (sample #3), 800 °C (sample #4) and 900 °C (sample #5). These samples were annealed in air and cooled in air. Sample #6 was obtained by annealing the as-grown sample at 900 °C and cooling in inert atmosphere (argon). Figure 1 shows the XRD pattern of the five samples (#1, #2 and #4 to #6) taken at 0.856 Å. XRD for sample #3 (annealed at 600 °C) was taken at slightly different wavelength (0.859 Å). A comparison of the measured XRD data with JCPDS data (No. 9-402) shows that samples #1 to #4 are a single-phase spinel structure ( $\text{Co}_3\text{O}_4$ ) with  $\text{Fm}\bar{3}\text{m}$  symmetry. Sample #5 annealed at 900 °C and cooled in air was a mixed  $\text{Co}_3\text{O}_4$  and  $\text{CoO}$  (fcc having  $\text{Fd}\bar{3}\text{m}$  symmetry) phase. Sample #6, annealed in air but cooled in inert atmosphere gives single  $\text{CoO}$  phase. We believe that spinel phase transforms to fcc phase for annealing temperature  $>850$  °C. Since sample #5 was cooled in air post-annealing, the fcc phase changes to spinel phase in the excess of air, while cooling. In order to verify this hypothesis, we cooled sample #6 in argon and got a single-phase  $\text{CoO}$  sample. We have conducted a high-resolution transmission electron microscopy (HRTEM) to ensure the crystalline quality of the nanoparticles. We see two parallel distinct atomic planes with  $d$  values 2.863 and 4.667 Å. These correspond to (111) and (220) planes of  $\text{Co}_3\text{O}_4$  phase and are in agreement with the XRD data (Fig. 1). In focused area, the planes are parallel with minimum visible defect-like dislocation. This shows that the method can be used for the synthesis of very good quality nanocrystals.

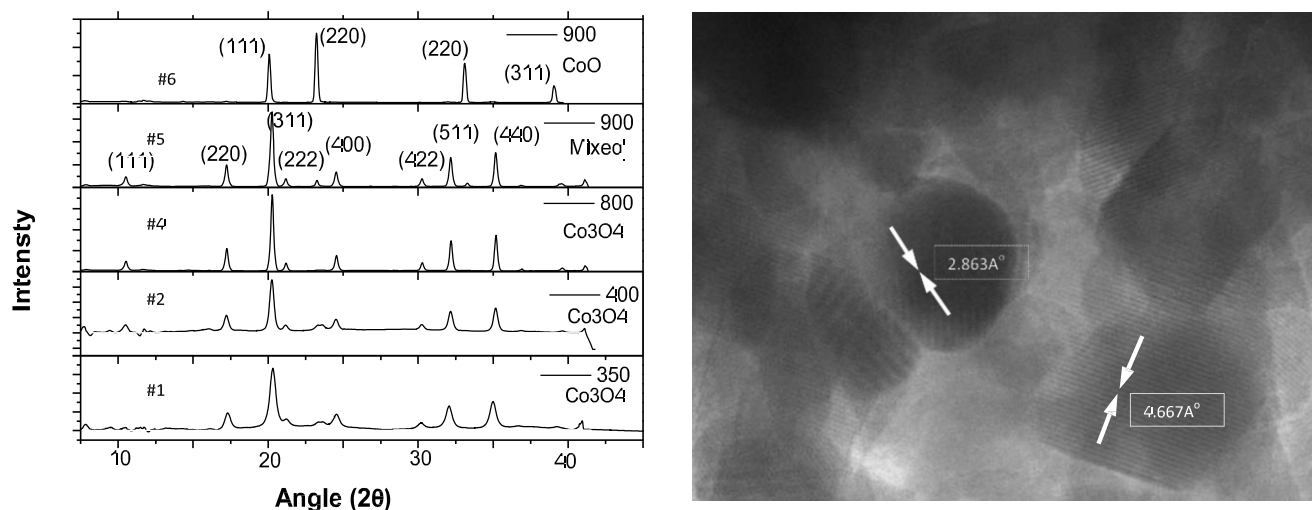


**Fig. 1** X-ray diffraction pattern for samples #1, #2, #4 to #6. Samples #1, #2 and #4 are single phase  $\text{Co}_3\text{O}_4$ , whereas sample #5 is mixed phase of  $\text{Co}_3\text{O}_4$  and  $\text{CoO}$  and sample #6 is pure  $\text{CoO}$  phase. Samples #5 and #6 are both annealed at  $900\text{ }^\circ\text{C}$  but sample #6 is cooled in inert atmosphere unlike other samples which are cooled in air.

A careful examination of XRD patterns of different samples in Fig. 1 shows that the lower diffracting planes like (111), (220) etc. for sample #1 are shifted towards higher  $2\theta$  values compared to those in samples #3 and #4; whereas the higher planes like (511), (440) etc. are shifted to lower  $2\theta$  values. This clearly shows lower  $d$  values of lower planes and higher  $d$  values of higher planes in the case of sample #1, compared to those in samples #3 or #4. Uniform strain or the macrostrain has been calculated by comparing the experimental  $d$  values for different samples with the tabulated values in the JCPDS data for the bulk. As discussed earlier, in order to accurately determine the  $d$  values, the X-ray wavelength was accurately determined by conducting the XRD on standard single crystal sample. All the measurements shown in Fig. 1 are taken in the same setting of area detector after wavelength was calibrated. The XRD data for sample #3 was taken at slightly different wavelength but after proper wavelength calibration. The wavelength in the two cases was  $0.856\text{ \AA}$  (Fig. 1). Each XRD peak was fitted using a Gaussian distribution and the position ( $2\theta$ ), and the FWHM were estimated. Interplanar distance  $d = \lambda/2 \sin \theta$ , thus obtained, was used to estimate the macrostrain =  $(d - d_{hkl})/d_{hkl}$ , where,  $d_{hkl}$  is the tabulated value of interplanar distance for (hkl) plane. Positive and negative values of the uniform strain give respectively elongation and compression strains. We find that the sample #1 (annealed at  $350\text{ }^\circ\text{C}$ ) has uniform compressive strain of  $0.4 \pm 0.05\%$  except for the planes (422) and (440) for which the compressive strains are lower ( $\sim 0.25\%$ ). For sample #2 (annealed at  $400\text{ }^\circ\text{C}$ ), the macrostrain for the lower planes is released, whereas the strain for the higher planes is comparable to that of sample #1. For sample #3 (annealed at  $600\text{ }^\circ\text{C}$ ) the macrostrain is annealed and the measured elongation strain is  $\sim 0.10\text{--}0.15\%$  for all the planes. The observation of these three samples is in agreement with the general understanding that the strain gets released on annealing. Here we add that the strain in lower planes is released first followed by the strain in higher planes. In the annealed state, the samples show slight elongation strain. It is further inferred that the best quality nanoparticles are obtained for annealing at  $600\text{ }^\circ\text{C}$ . This is in agreement with our optical absorption data (to be discussed later). Annealing at higher temperatures again shows higher compressive strain. We

believe that this may be because when annealing at higher temperatures ( $\geq 800$  °C), mixed phases of spinel and fcc nanoparticles are synthesized. For sample #4, annealed at 800 °C, the amount of minor fcc phase is too low to be detected by XRD. For sample #5, annealed at 900 °C, the minor phase is detected by XRD (see Fig. 1). This result is also corroborated by sub-gap absorption measurements (to be discussed later in Sect. 3.2) on these samples.

### 3.2 Optical overview

Both the macro- and the micro-strain induce localized density of states (DOS) in the band gap, thereby increasing the sub-gap absorption. The origin of macrostrain is change in bond length, bond angle distortion, etc. These distortions give rise to increase in the slope of band tail (called Urbach edge). The origin of microstrain, on the other hand is in defects like point-defect, dislocation, etc. These defects induce DOS in the mid-gap region. Sub-gap absorption is a fundamental process, which measures the density as well as energy positions of all the states in the band gap. As described in Experimental section, the transmission measurements in these particles have been conducted by suspending the particles in liquid. Transmission thus obtained has been corrected for scattering because of change in wavelength (Rayleigh scattering) and particle size. We find that the slope of the sub-gap absorption curve increases for samples #1 to #3. A first impression is that there is decrease in density of states and hence the strain in the sample, as the samples are annealed at higher temperatures. This is in agreement with both macro- and micro-strain estimated using XRD data. For samples #4 and #5 annealed at temperatures 800 and 900 °C, respectively, the absorption curves in the sub-gap region are almost flat. This can happen if the samples are mixed phases and the band gap of the minor phase is different from the major phase. For sample #5, the mixed phase is clearly seen in XRD measurements (see Fig. 1). We believe that the sample #4 is also a mixed-phase sample but the minor (CoO) phase is too small to be detected in the XRD measurements.

In order to quantitatively compare density of states (DOS) in the band gap for samples #1 to #3, we estimate DOS for these samples from the sub-gap absorption data. We assume parabolic conduction and valence band states given by  $N(E) = N_E \cdot E^{1/2}$ . The DOS near the band edges vary exponentially and the origin of these states are variations in bond angle and bond length. This is called the Urbach edge and is assumed to be the same ( $E_0$ ) for conduction as well as valence band edges for these calculations. The variations in the bond length and bond angle are also the origin for macrostrain.

## 3. CONCLUSIONS

Two stable phases of cobalt oxide (Co<sub>3</sub>O<sub>4</sub> and CoO) nanoparticles were synthesized using environmentally friendly inorganic precursor, by wet chemical route. Sizes of the nanoparticles were found to increase with increasing annealing temperature. Macro- and micro-strain in the samples were estimated by analysis of XRD peak position and FWHM, respectively. Macrostrain was found to be the minimum for particles annealed at 600 °C. We attribute the increase in microstrain for the samples annealed at  $\geq 800$  °C to the appearance of mixed phase in the sample. DOS in the band gap was estimated using sub-gap absorption measurements. It was found that both slope of Urbach edge and the mid-gap states ( $N_G$ ) decrease for samples #1 to #3. DOS in the band gap, therefore, is found to correlate well with the change in macro- as well as micro-strain for the samples. This is justified because

lattice defects like dislocation, point-defect, distorted grain boundaries, bond angle/length variations, etc. contribute to both strain and localized DOS in the band gap.

## References

- [1] H.K. Lin, H.C. Chiu, H.C. Tsai, S.H. Chien, C.B. Wang, *Catal. Lett.* 88 (2003) 169
- [2] H. Yamaura, K. Moriya, N. Miura, N. Yamazoe, *Sens. Actuators B* 65 (2000) 39
- [3] S.A. Makhlof, *J. Magn. Mater.* 246, 184 (2002) 4. T. Zhu, J. Luo, J.K. Liang, G.H. Rao, J.B. Li, J.Y. Zhang, Z.M. Du, *Physica, B* 403 (2008) 3141
- [5] J.G. Cook, F.P. Koffyberg, *Sol. Energy Mater.* 10 (1984) 55
- [6] T. Seike, J. Nagal, *Sol. Energy Mater.* 22 (1991) 107
- [7] P. Poizot, S. Larulle, S. Grugeon, L. Dupont, M. Tarascon, *Nature* 407 (2000) 496
- [8] G.X. Wang, Y. Chen, K. Konstantinov, M. Linsey, H.R. Liu, S.X. Dou, *J. Power Sources* 109 (2002) 142
- [9] G.H. Jaffari, H.Y. Lin, C. Ni, S.I. Shah, *Mater. Sci. Eng. B* 164 (2009) 23
- [10] R. Riva, H. Meissner, R. Vitali, G.D. Piero, *Appl. Catal. A* 196 (2000) 111
- [11] L. Zhang, D. Xue, G. Gao, *J. Magn. Mater.* 267 (2003) 111
- [12] L. Neel, C. Dewitt, B. Dreyfus, P.D. de Gennes (eds.), *Low Temp. Phys.* (Gordon and Breach, New York, 1962) p. 413
- [13] R.K. Gupta, A.K. Sinha, B.N. Raja Sekhar, A.K. Srivastava, G. Singh, S.K. Deb, *Appl. Phys. A* 103 (2011) 13
- [14] P.W. Anderson, *Phys. Rev.* 109 (1958) 1492
- [15] N. Mott, E.A. Davies, *Electronic Processes in Non-crystalline Materials* (Cambridge University Press, Cambridge, 1979).
- [16] A.K. Sinha, A. Sagdeo, P. Gupta, A. Kumar, M.N. Singh, R.K. Gupta, S.R. Kane, S.K. Deb, *Proceedings of the 55th DAE Solid State Physics Symposium*. AIP Conf. Proc., vol. 1349 (2011).
- [17] G. Singh, X. Abdurahim, A. Banerji, K. Barpande, V. Bhatnagar, A.G. Bhujle, A.A. Fakhri, P. Fatnani, A.D. Ghodke, P.R. Han- nurkar, A.C. Holikatti, R. Husain, S.K. Jena, P. Kant, S. Kota- iah, P. Kumar, M. Lad, R.G. Marathe, M. Pravinkumar, T.A. Pun- tambekar, V.C. Sahni, R.S. Saini, A. Sharma, R. Shridhar, S.K. Shukla, A.C. Thakurta, A.P. Thipsay, S.R. Tiwari, D.S. Thakur, D.K. Vats, *Proceedings of the Indian Particle Accelerator Conference* (2006).
- [18] G.K. Williamson, W.H. Hall, *Acta Metall.* 1 (1953) 122
- [19] Y. Zhao, J. Zhang, *J. Appl. Crystallogr.* 41 (2008) 1095
- [20] P.B. Belavi, G.N. Chavan, L.R. Naik, *Mater. Chem. Phys.* 133 (2012) 138
- [21] Y. Yin, A.P. Alivisatos, *Nature* 437 (2005) 664

© 2021 The Authors. Published by SIATS (<http://etn.siats.co.uk/>). This article is an open access article distributed under the terms and conditions of the Creative Commons Attribution license (<http://creativecommons.org/licenses/by/4.0/>)